Geoscience Frontiers 10 (2019) 2135–2145

HOSTED BY

Contents lists available at ScienceDirect

China University of Geosciences (Beijing)

Geoscience Frontiers

journal homepage: www.elsevier.com/locate/gsf

Research Paper

Quantifying a critical marl thickness for vertical fracture extension using field data and numerical experiments

Filiz Afşar [a,b,*], Elco Luijendijk [c]

[a] Kalkulo AS, Simula Research Laboratory, Martin Linges vei 17, Fornebu, 1364, Norway
[b] Department of Earth and Planetary Sciences, University of California, Riverside, 900 University Avenue, California, 92521, USA
[c] Department of Structural Geology and Geodynamics, University of Göttingen, Goldschmidtstrasse 3, 37077, Göttingen, Germany

ARTICLE INFO

Article history:
Received 31 July 2018
Received in revised form
24 April 2019
Accepted 23 May 2019
Available online 7 June 2019

Keywords:
Boundary element modelling
Marl/limestone multilayer
Layer thickness and stiffness control
Permeability
Fractured reservoirs

ABSTRACT

In fractured reservoirs characterized by low matrix permeability, fracture networks control the main fluid flow paths. However, in layered reservoirs, the vertical extension of fractures is often restricted to single layers. In this study, we explored the effect of changing marl/shale thickness on fracture extension using comprehensive field data and numerical modeling.

The field data were sampled from coastal exposures of Liassic limestone-marl/shale alternations in Wales and Somerset (Bristol Channel Basin, UK). The vertical fracture traces of more than 4000 fractures were mapped in detail. Six sections were selected to represent a variety of layer thicknesses. Besides the field data also thin sections were analyzed. Numerical models of fracture extension in a two-layer limestone-marl system were based on field data and laboratory measurements of Young's moduli. The modeled principal stress magnitude σ_3 along the lithological contact was used as an indication for fracture extension through marls. Field data exhibit good correlation ($R^2 = 0.76$) between fracture extension and marl thickness, the thicker the marl layer the fewer fractures propagate through. The model results show that almost no tensile stress reaches the top of the marl layer when the marls are thicker than 30 cm. For marls that are less than 20 cm, the propagation of stress is more dependent on the stiffness of the marls. The higher the contrast between limestone and marl stiffness the lower the stress that is transmitted into the marl layer. In both model experiments and field data the critical marl thickness for fracture extension is ca. 15–20 cm.

This quantification of critical marl thicknesses can be used to improve predictions of fracture networks and permeability in layered rocks. Up- or downsampling methods often ignore spatially continuous impermeable layers with thicknesses that are under the detection limit of seismic data. However, ignoring these layers can lead to overestimates of the overall permeability. Therefore, the understanding of how fractures propagate and terminate through impermeable layers will help to improve the characterization of conventional reservoirs.

1. Introduction

Unconventional reservoirs have become a significant source of hydrocarbon production within the last decades. The technically recoverable unconventional resources worldwide are estimated at 7059 trillion cubic feet (tcf) (e.g., Gale et al., 2014). Such reservoirs have, however, a poor matrix-permeability and therefore fluid flow is largely controlled by the connectivity of their fracture networks (e.g., Aguilera, 2000; Economides and Nolte, 2000; Brenner and Gudmundsson, 2004; Larsen and Gudmundsson, 2010).

Technologies like hydraulic fracturing can increase the permeability in such reservoirs. The advancement in drilling technology over the last ten years made meter-scale targeting of reservoirs possible. However, the smaller the scale in the subsurface, the more difficulties and uncertainties arise in the characterization of unconventional reservoirs. High-resolution seismic data, for example, can resolve only near surface features thicker than 10 m with a 2000 ms^{-1} velocity and 50 Hz frequency (Yilmaz, 2001). In contrast,

* Corresponding author. Kalkulo AS, Simula Research Laboratory, Martin Linges vei 17, Fornebu, 1364, Norway.
E-mail address: dr.filiz.afsar@gmail.com (F. Afşar).
Peer-review under responsibility of China University of Geosciences (Beijing).

https://doi.org/10.1016/j.gsf.2019.05.008

bore-hole images provide details in mm to cm scale, however, these do not cover spatial variability. The lack of information and the existing heterogeneities in such scales hamper the upscaling of permeability to reservoir scales.

In unconventional reservoirs, the permeability is often increased by injecting fluids under high-pressure. This increases the connectivity of pre-existing natural fractures (i.e. '>hydraulic stimulation') or generates new fractures (i.e. 'hydraulic fracturing') (Economides and Nolte, 2000). Fractures formed by hydraulic fracturing may also propagate vertically through adjacent layers and can reactivate pre-existing fractures. Due to these unexpected pathways, fluids (like drill mud) can leak out in the corresponding formation (Mitchell, 2006). The predictability of fracture networks is, accordingly, more difficult, particularly the interaction between man-made fractures and pre-existing natural fracture networks. Therefore, the study of natural fracture systems is important for a better prediction of hydraulic fractures during stimulation. In addition, microseismic events associated with hydraulic-fracture stimulation have been ascribed not only to natural fracture reactivation but also to differential stress accumulation between mechanically soft and stiff layers (Roche and Baan, 2013; Gale et al., 2014). Therefore, the understanding of fracture extension within soft marl in limestone-marl alternation is especially important to minimize the risk of microseismic events while fracturing. This issue is of public interest, especially when fracking fluids flow through unexpected fracture paths and contaminate water in aquifers or trigger microseismic events, which happens in the past; e.g. while extracting natural gas from Marcellus Shales or Barnet Shales in the U.S. (e.g., Zoback et al., 2010; Rozell and Reaven, 2012). The characteristics of fracture networks are thus key parameters to improve not only well performance but also to provide more accurate reservoir models. Limestone-marl alternations frequently contain oil-shale beds where hydrocarbons are generated, stored and trapped, as in the case of oil-shale beds of the Blue Lias Formation (Harvey and Gray, 2013). Especially, the study area around Somerset is recently in commercial interest. Eight Petroleum and Exploration Development Licences (PEDLs) blocks were signed in September 2016 held by South West Energy (Somerset County Council, 2017). In such layered rocks, the natural vertical fracture permeability varies considerably from layer to layer due to the change of mechanical properties between layers and interfaces (Aguilera, 2000). When fractures are contained within one bed bounded by impermeable layers, such a bed is considered to be one flow unit (National Research Council, 1996). Once a fracture crosses from one flow unit into the next, the two units may be connected, and the drainage volume increases (Rijken and Cooke, 2001). Ignoring the variation in permeability between these layers can lead to miss estimates of its overall permeability (Aguilera, 2000).

Our goal is to quantify the relation between marl/shale thickness and the vertical fracture extension, using a combination of field/laboratory studies and numerical experiments. We investigated the vertical fracture extension through limestone-marl/shale alternations and detected more than 4000 fractures within six sections in Wales and Somerset (Bristol Channel Basin, UK). Fractures over several layers in six sections were traced, belonging to the Blue Lias Formation (Lower Jurassic, Hettangian-Sinemurian). The focus in this study is on the vertical continuity of fractures, whereas previous studies focused on fracture distribution (fracture density and spacing in limestone-marl alternations) and the effect of diagenesis on fracture mechanics (Afşar et al., 2014). Upscaling methods often ignore spatially continuous extremes, like impermeable layers such as shale or marl barriers (Qi and Hesketh, 2005). Detailed understanding of fracture extension and termination in impermeable layers in natural systems will help to improve the prediction of hydraulic fracture networks and permeability in these systems.

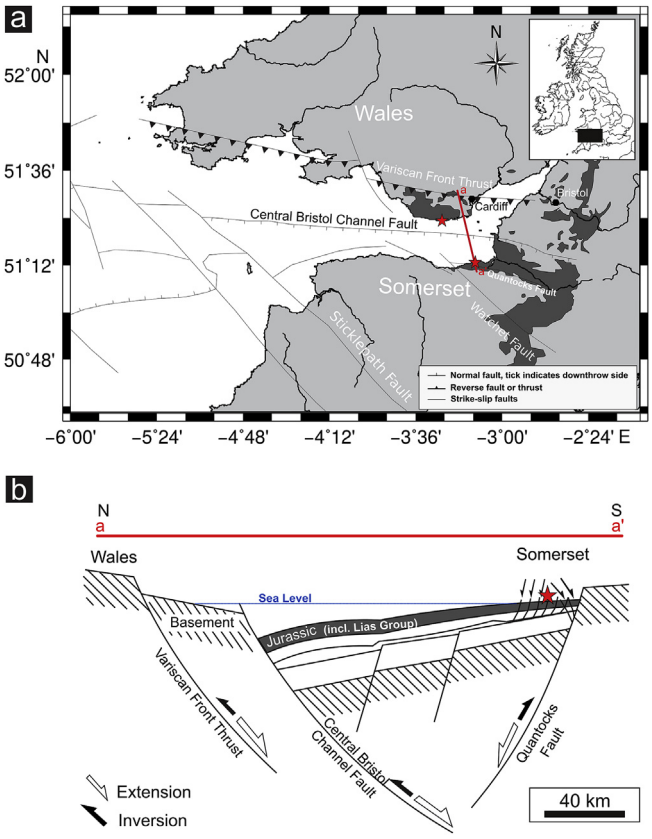

Figure 1. Geographic and tectonic overview of the study area. (a) Location of the two study areas (stars) with an outcrop map of the Lias Group (dark grey) (modified after Kamerling (1979), Tappin et al. (1994), Cox et al. (1999), Belayneh and Cosgrove (2010)); (b) sketch cross-section of the Bristol Channel Basin. The Lias Group is a part of the Jurassic strata. The exact location of the cross-section is estimated (adapted from Stewart et al., 1997).

2. Geological setting

The succession of the Blue Lias Formation (Hettangian-Sinemurian) is well-exposed along the coastline of the Bristol Channel (UK; Fig. 1a) and comprises limestone-marl and/or -shale alternations with thicknesses of 150 m in South Wales (Wilson, 1990) and 175 m in North Somerset (Whittaker and Green, 1983). The Blue Lias Formation was deposited in the Bristol Channel Basin, which is an asymmetric graben, bounded to the north by the Variscan Front Thrust Fault (e.g., Hoorn, 1987, Fig. 1b). The recent structure of the Bristol Channel Basin is the result of a complex tectonic history (Kamerling, 1979), though the architecture of the basin is mostly controlled by the Variscan orogeny (Hoorn, 1987; Brooks et al., 1988). Development of the Bristol Channel Basin started during the Permo–Triassic Rifting with an N–S extension direction, which reactivated the Hercynian Thrust Zone (Hoorn, 1987). As a consequence of NE–SW to NNE–SSW extension during Late Triassic and Jurassic, regional subsidence of the basin took place (Dart et al., 1995; Nemčok et al., 1995). These processes are reflected by gradual marine transgression (Wilson, 1990). As a consequence, shallow marine near-shore facies directly overlie the Upper Palaeozoic basement in the area of South Wales (Donovan et al., 1979). The major fault systems along the basin margins were active during the Mesozoic N–S extension, which is indicated by 095°-striking

normal faults (e.g., Kamerling, 1979; Hoorn, 1987). Many of these normal faults were reverse-reactivated in strike-slip mode during the late Cretaceous and early Tertiary compression (e.g., Dart et al., 1995; Nemčok et al., 1995). Reverse faulting was more prevalent on the southern margin (Somerset) than on the northern margin (Wales) of the Bristol Channel Basin (Nemčok et al., 1995).

3. Methods

3.1. Field data and laboratory work

The vertical extent of more than 4000 fractures within six sections was sampled in a 15 m × 2 m window, three sections in Wales (Sections: NP1-3) and three in Somerset (Sections: KI1, LIL2, KN3; Fig. 1a). The vertical traces of fractures were documented with their extension on 64 lithological contacts and through 63 layers. The sections were selected to represent a variety of marl and shale thicknesses. The lithologies were distinguished in respect of potential mechanical stress barriers, e.g. laminated marl and regular marl.

We modified the well-known scan-line method, described in Zeeb et al. (2013) for our purpose of measuring the fracture traces through several layers as described in Afşar et al. (2014). With the scan-line method, fractures with smaller than 0.1 mm aperture could be measured, which are below the detection limits of digital technologies. Since for short fractures measurement errors (in particular of the strike) increase progressively, only fractures with heights larger than 7 cm are included in the data set. For layers that are less than 7 cm thick, the threshold of 7 cm was lowered to 4 cm. The scan-lines were 15 m long and oriented parallel to the bedding and perpendicular to the main fracture set. The beds within the 15 m were named in alphabetical order. Each fracture was classified in seven groups with respect to its trace (Fig. 2a). In this study, we differentiate between fracture traces through marl layers (non-stratabound vs. stratabound fractures; Fig. 2b) and fracture traces along limestone-marl contacts (fracture crossing vs. termination; Fig. 2c). Fracture parameters geometry (strike, dip, height) were recorded (Afşar et al., 2014). For each fracture, the local bed thickness was measured. Sedimentological fieldwork included the measurement of six detailed sedimentary sections and the documentation of important sedimentary features in bed-scale.

In addition, 59 thin sections were analyzed under transmitted- and polarized light. $CaCO_3$ and C_{org} contents were measured on 64 samples with a Hekatech Euro Elemental Analyzer (CNS; Table 1). Young's moduli (E) were measured for two different types of limestone that were found in the study area, well-bedded limestones with relatively planar and semi-nodular limestones with wavy surfaces. Because of the high fragility of marls, a sampling of large rock blocks was limited for marl layers. The Young's modulus describes the stiffness of rocks and can be defined as the ratio of stress to strain, provided that the rock behaves linear elastic, which is the case at low temperatures and pressures (Hooke's law; cf. Hudson and Harrison, 2000). To consider variations of strength and stiffness within the same layer, a minimum of six specimens for each lithology was measured parallel and perpendicular to sedimentary bedding. The specimens for the uniaxial compression test were prepared according to Hudson et al. (2003). During a constant loading rate of 0.5 MPa s^{-1}, stress and strain were recorded until the failure of the specimens occurred. The static Young's modulus is determined from the stress-strain curve after a pre-load of about 70% of UCS. The average values of Young's modulus for two limestones were used later for the numerical model experiments.

3.2. Numerical models

We performed numerical experiments of fracture extension in a two-layer limestone-marl system using the boundary element model code Beasy (Beasy, 1991; Brebbia and Dominguez, 1994), which uses the dual boundary element method (Portela et al., 1993). The model code was used to calculate the stress distribution in the marl layer resulting from a tensile stress applied to a single fracture in a limestone layer underneath.

The model domain consists of a 100 cm thick limestone in which the fracture is hosted. The limestone is overlain by marls of which the thickness was varied between different model experiments. Young's modulus for the limestone unit (40 GPa) was assigned based on the average of two measured samples taken from the field (see Section 3.1.). Poisson's ratio ($\nu = 0.34$) was based on literature sources measured on fine-grained argillaceous limestones of the Blue Lias Formation (Hobbs et al., 2012). The effects of marl thickness and stiffness on fracture extension were assessed using several model experiments, which are listed in Table 2. The model setup is

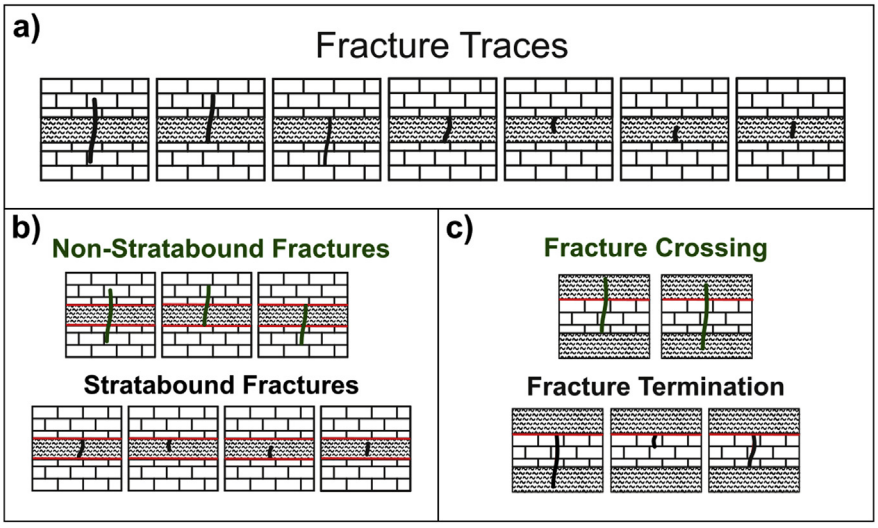

Figure 2. (a) Overview of seven different fracture traces. The fractures were distinguished between fracture traces through marls (b) non-stratabound vs. stratabound fractures and fracture traces through limestone-marl contacts (c) fracture crossing vs. termination.

Table 1
Lithology, average bed thickness, $CaCO_3$ and C_{org} content of each bed collected in all sections. WBL = well-bedded limestones, SNL = semi-nodular limestones, CM = calcareous marls, LCM = laminated calcareous marls, LM = laminated marls, RM = regular marls. Please note that all sections represent different stratigraphic intervals within the Blue Lias Formation. Fracture terminations of NP1, and NP2 are shown in Fig. 12.

		Layers												
		A	B	C	D	E	F	G	H	I	J	K	L	M
NP1	Lithology	LM	SNL	CM	WBL	LM	WBL	CM	WBL	CM	WBL	RM	SNL	RM
	Thickness (cm)	15	10	7	18	13	11	6	11	5	17	20	8	13
	$CaCO_3$ (wt.%)	25	86	59	83	31	85	64	81	52	78	46	74	56
	C_{org} (wt.%)	1.29	0.25	0.64	0.24	1.63	0.25	0.50	0.29	0.60	0.32	0.99	0.51	0.83
NP2	Lithology	WBL	RM	LM	WBL	LCM	SNL	LCM	SNL	LCM	WBL	RM	LM	WBL
	Thickness (cm)	49	5	6	27	5	6	5	11	5	26	5	15	37
	$CaCO_3$ (wt.%)	50	27	29	89	51	74	48	82	44	89	41	56	72
	C_{org} (wt.%)	0.54	0.73	1.10	0.23	0.62	0.24	0.61	0.21	0.56	0.21	1.07	2.15	0.32
NP3	Lithology	RM	SNL	RM	SNL	RM	WBL	CM	SNL	CM	SNL	RM	SNL	
	Thickness (cm)	7	6	16	16	23	24	7	10	8	12	13	11	
	$CaCO_3$ (wt.%)	41	82	51	84	33	79	59	86	65	92	33	81	
	C_{org} (wt.%)	1.03	0.27	0.46	0.20	0.74	0.33	0.55	0.47	0.37	0.18	0.96	0.28	
KL1	Lithology	RM	SNL	LCM	LM	SNL	CM	LM	CM	WBL				
	Thickness (cm)	28	14	23	29	16	7	43	11	12				
	$CaCO_3$ (wt.%)	42	86	57	26	78	55	36	50	82				
	C_{org} (wt.%)	0.72	0.24	0.90	7.12	0.73	0.57	15.73	2.47	0.48				
LIL2	Lithology	WBL	LCM	WBL	CM	WBL	CM	LM	WBL	CM	SNL			
	Thickness (cm)	18	9	21	6	19	5	27	13	7	11			
	$CaCO_3$ (wt.%)	82	52	84	59	77	48	36	82	52	84			
	C_{org} (wt.%)	0.32	0.73	0.36	0.70	0.46	0.87	3.34	0.27	1.01	0.28			
KN3	Lithology	LM	WBL	LM	SNL	CM	WBL							
	Thickness (cm)	36	16	18	11	11	21							
	$CaCO_3$ (wt.%)	40	83	47	86	47	80							
	C_{org} (wt.%)	0.95	0.24	1.58	0.26	0.91	0.33							

shown in Fig. 3. The marl thicknesses (1–30 cm) were based on own field observations. Young's moduli for marls were varied from 2 GPa (i.e., soft) up to 30 GPa (i.e., stiff), in rough accordance with values in marls from the Lias mudstone (<35 GPa; Reeves et al., 2006). Since the Poisson's ratio of different marls varies only within a small range (0.3–0.33: Dvorkin et al., 2005), the same Poisson's ratio ($\nu = 0.34$) like the limestone was chosen.

A vertical opening-mode fracture is hosted in the limestone with an extension to the horizontal interface representing the contact between limestone and marl (Fig. 3). Perpendicular to the fracture, the effective horizontal tension of 10 MPa was applied to simulate a tensile fracture at less than 400 m at depth (Fig. 3), in accordance with estimated burial depth of the Blue Lias Formation, when the first joint set was formed (Late Oligocene to Miocene; cf. Cornford, 1986). When the tensile stress exceeds the tensile strength of the rock, new fractures were initiated, or existing fractures propagated across the contacts (Jaeger et al., 2007). Parameters like pore pressure or regional stress field are not considered in this numerical experiment. The model is constrained by parameters, like Young's modulus E, Poisson's ratio ν, and marl thicknesses. For this model the assumption of linear elastic rock behavior was made, i.e. Young's modulus (E) of that rock can be defined as the ratio of stress to strain (Hooke' law), which might not be very accurate when considering very soft marls (Jaeger et al., 2007; Zoback, 2007).

4. Results

4.1. Field and laboratory data

Two limestone lithologies were classified following the degree of nodularity of the bedding planes that was observed in the field: well-bedded limestones with relatively planar surfaces (WBL) and semi-nodular limestones with a wavy surface at the top and/or at the base (SNL). Following the Dunham (1962) classification, both lithologies are characterized by wackestones and, more predominantly, mudstones. Apart from a few macro-and microfossils in some beds, the successions are generally devoid of fossils.

Four different marl lithologies were classified by weathering color and $CaCO_3$ content: calcareous marls (CM; Fig. 4a) and laminated calcareous marls (LCM; Fig. 4b) were both characterized by a light grey weathering color, whereas regular marls (RM; Fig. 4c) and laminated marls (LM; Fig. 4d) were characterized by a dark grey weathering color. LCMs or LMs are indicated by laminae observed in the field or thin sections (Fig. 4b,d). $CaCO_3$ content of CMs and LCMs ranges from 44 wt.% to 82 wt.%; both are slightly higher than the content of RMs and LMs (25–56 wt.%) (Table 1). Within some marls, sharply defined color changes, from light grey to dark grey, occur along strongly bioturbated transitions (*Chondrites* type; Fig. 5a and b). Thin sections reveal that these bioturbation tubes are

Table 2
Modelled values of marl thickness H (cm) and marl stiffness E (GPa). For model experiments H02E02, H05E02, H02E10, H05E10, H02E20, H05E20 the modelled tensile stresses are shown in Fig. 11.

		Marl thickness H (cm)							
		01	02	05	10	20	30	40	50
Marl stiffness	2	H01E02	**H02E02**	**H05E02**	H10E02	H20E02	H30E02	H40E02	H50E02
E (GPa)	5	H01E05	H02E05	H05E05	H10E05	H20E05	H30E05	H40E05	H50E05
	10	H01E10	**H02E10**	**H05E10**	H10E10	H20E10	H30E10	H40E10	H50E10
	20	H01E20	**H02E20**	**H05E20**	H10E20	H20E20	H30E20	H40E20	H50E20
	30	H01E30	H02E30	H05E30	H10E30	H20E30	H30E30	H40E30	H50E30

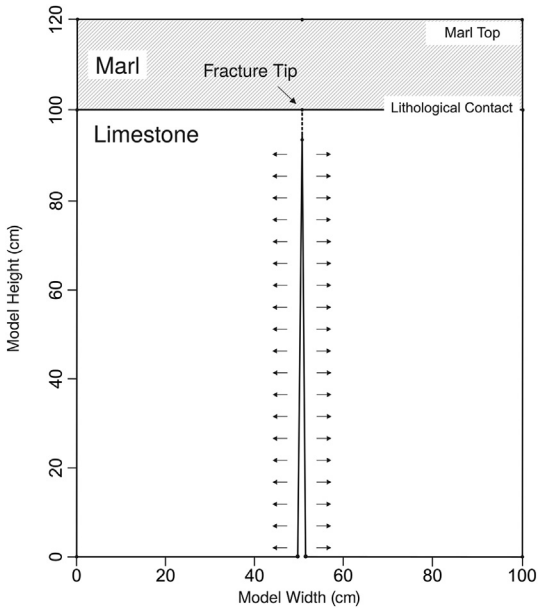

Figure 3. Overview of the model domain used for the model experiments. The limestone has a thickness of 100 cm and Young's modulus of E = 40 GPa. The fracture is hosted in the limestone and terminates at the lithological contact (fracture tip). The stress magnitude and distribution at the marl top were investigated with changing marl thickness H (cm) and Young's modulus E (GPa) (see Table 2 for an overview of the model parameter).

ubiquitous within calcareous marls (Fig. 5b). These marls/shales are rich in organic carbon (up to 16 wt.% C_{org}), as evidenced by the dark color in the outcrop (Fig. 5c and d).

The percentage of fracture terminations at the top and at the bottom of each limestone was plotted against the marl thickness (H) of either the marl above or below (Fig. 6). Hence, each of the plotted 67 points represents a limestone-marl contact. Additionally, we distinguished different types of marls which are referring to the marl above and below (see the legend in Fig. 6a). The different marl lithologies represent a relative marl stiffness (e.g. calcareous marl as stiff and regular marl as soft layer). This plot clearly shows that fracture termination is not correlated with marl thickness ($R^2 = 0.04$).

Fig. 7 shows the number of fracture terminations and crossings through all lithological contacts. The total number of lithological contacts is 128. Note that each contact is counted twice because the layer top is at the same time the layer bottom of the layer above. Fig. 7b shows the situation in the field, however, in this sketch only for the limestone-marl contact. More than half of the lithological contacts show higher amounts of fracture terminations than crossings (see 50% line in Fig. 7a).

Fig. 8 shows the percentage of fractures that extend vertically through different marl types and thicknesses. Each point represents one marl, which is in total 29 (Fig. 8a). In this study, we defined stratabound fractures as restricted to individual layers and non-stratabound fractures as non-restricted (and if restricted than either at the top or at the bottom of one layer; Fig. 8b). The data show that the percentage of non-stratabound fractures has a strong correlation ($R^2 = 0.76$) with the marl thickness (cm) (Fig. 8a).

The sections are divided between the northern part (foot-wall in Wales; Figs. 1b, 9a–c) and the southern part (hanging-wall in Somerset, Figs. 1b, 9d–f) of a half-graben. Fig. 9 shows rose diagrams of all fractures, revealing two main strike directions in Wales (~E–W and ~N–S; Fig. 9a–c) and in Somerset (~NW–SE and ~NE–SW; Fig. 9d–f). In Wales the range of fracture strikes is narrow, whereas in Somerset the range of strikes much wider (Fig. 9).

4.2. Numerical experiments

The results of the model experiments show that the maximum stress ratio between the marl top and bottom is highly dependent on its thickness. The stress ratio decreases rapidly between a thickness of 1 cm and 10 cm thick marls and drops steadily with greater than 10 cm thick marls (Fig. 10). Almost no tensile stress reaches the top of marls when the marls are thicker than 30 cm (Fig. 10). For marls that are less than 20 cm, the propagation of stress is also dependent on the stiffness of the marls (Fig. 10).

In addition to the thickness of the marls, the contrast in stiffness between limestones and marls affects the tensile stress in marl layers (see stress ratio at 1 cm thick marls, Fig. 10). The higher the

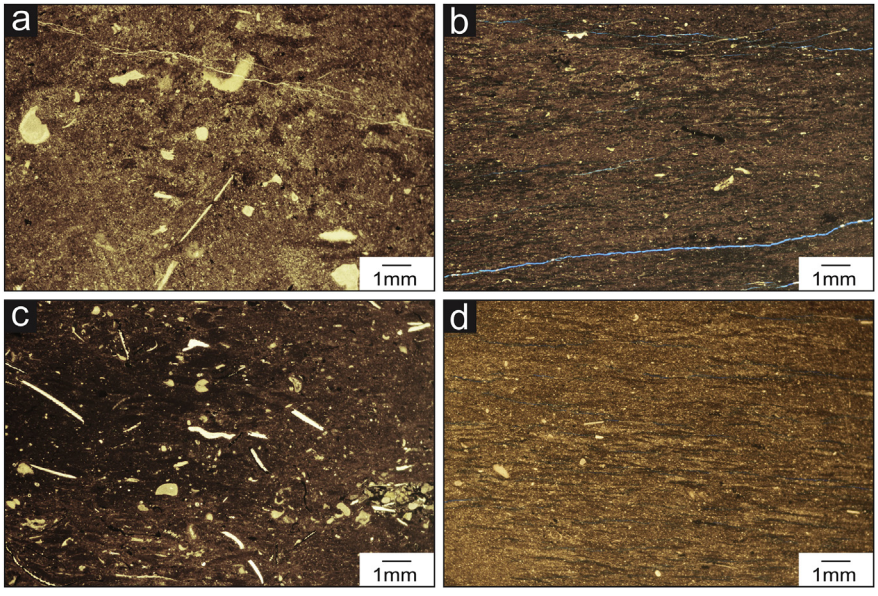

Figure 4. Four thin sections of each marl lithology: (a) calcareous marl, (b) laminated calcareous marl, (c) regular marl, (d) laminated marl.

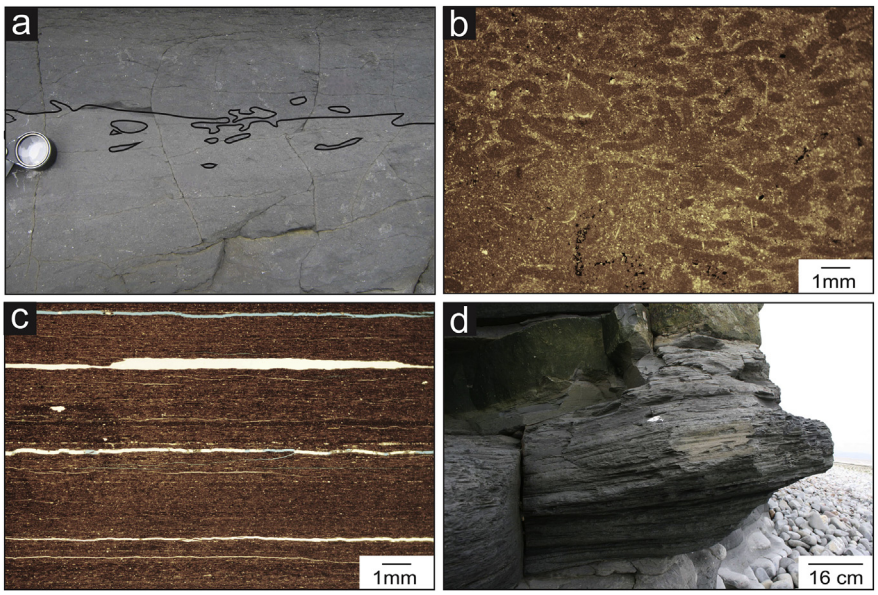

Figure 5. Characteristics of marls: (a) and (b) bioturbation within calcareous marls (lens as scale in a), C_{org} rich shale (16 wt.%) in (c) thin section and (d) outcrop.

contrast between limestone (40 GPa) and marl stiffness (dark blue line for 2 GPa in Fig. 10), the lower the stress that is transmitted into the marl layer to the marl top, independent of its thickness (see Fig. 10, Marl thickness from 1 cm to 10 cm; and contour lines in Fig. 11a and b).

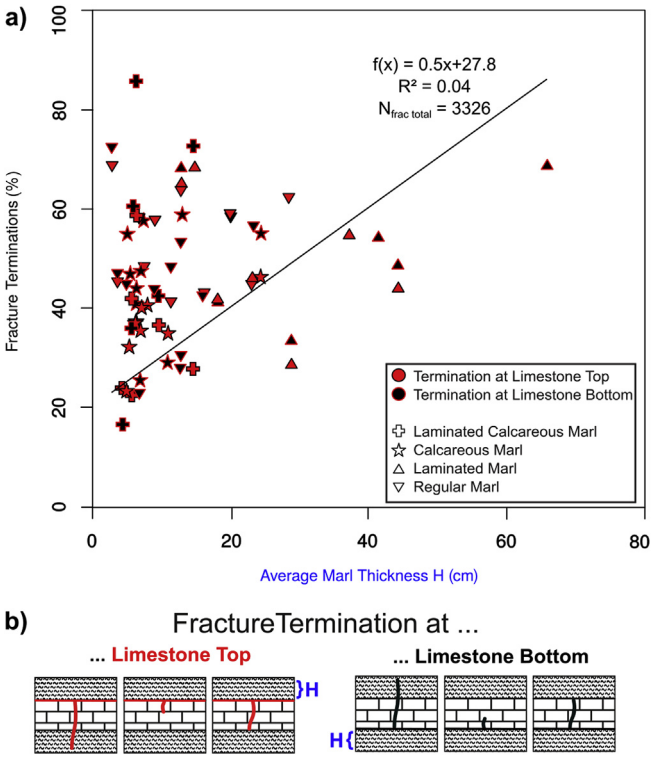

Figure 6. (a) The percentage of fracture terminations (%) at the top (in red) and at the bottom (in black) of each limestone-marl contact is plotted against the average marl thickness (H) (cm). The symbols represent four different marl lithologies, which represent a relative marl stiffness (e.g. calcareous marl as stiff layer and regular marl as soft layer; see symbols). The total number of fractures ($N_{frac\ total}$) in this plot is 3326 (i.e. fracture terminations and crossings through each contact). (b) The sketch illustrates the situation in the field.

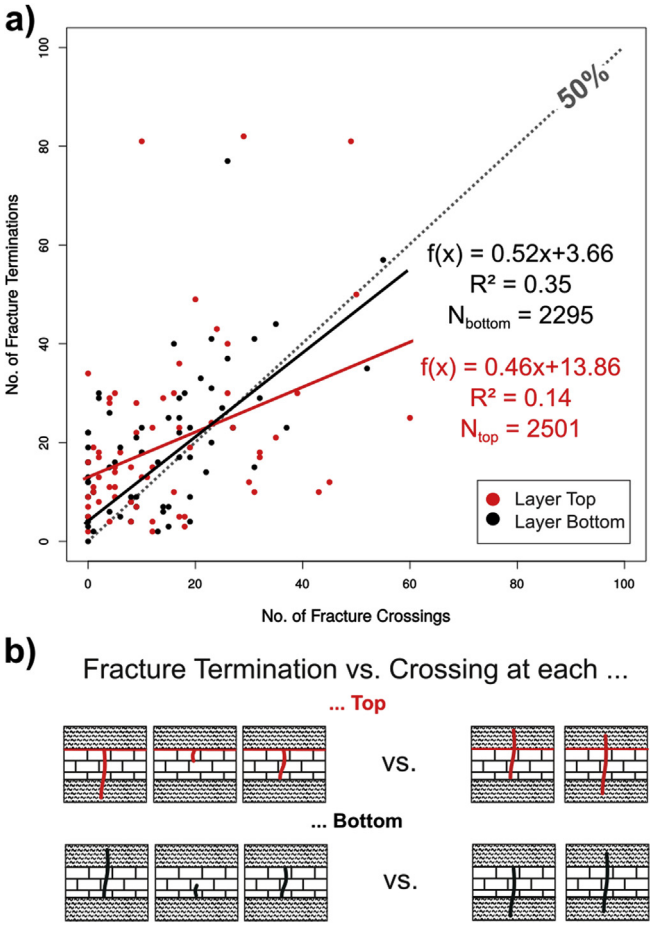

Figure 7. (a) Number of fracture terminations and fracture crossings through all lithological contacts ($N_{contact} = 128$) are illustrated here. The total number of fracture terminations and crossings for all layer tops is 2501 (N_{top}) and for all layer bottoms 2295 (N_{bottom}). (b) The sketch illustrates the situation in the field.

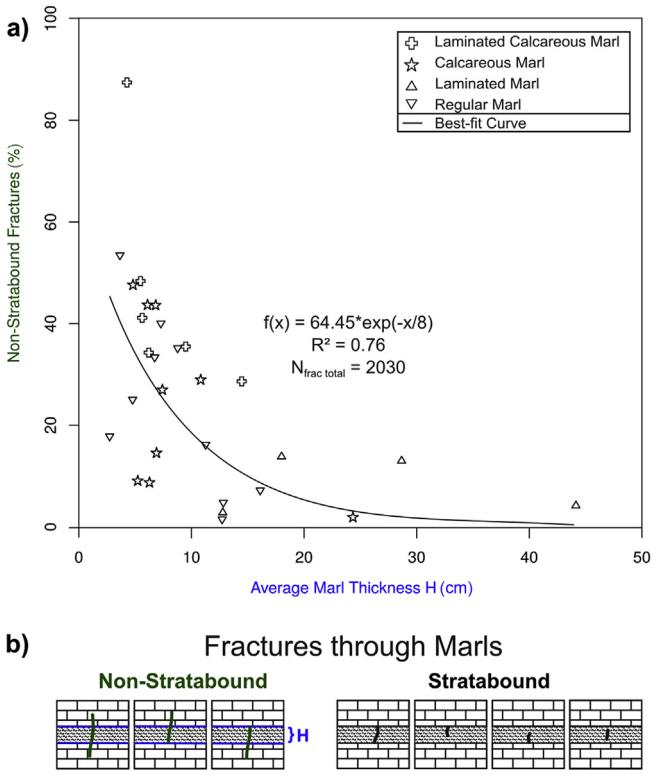

Figure 8. Cross-plot of non-stratabound fractures (%) and marl thickness (cm). The symbols represent four different marl lithologies, which represent a relative marl stiffness (e.g. calcareous marl as stiff and regular marl as soft layer; see symbols). The total number of fractures ($N_{frac\ total}$) in this plot is 2030 (i.e. non-stratabound and stratabound fractures; Fig. 9b). (b) The sketch illustrates the situation in the field.

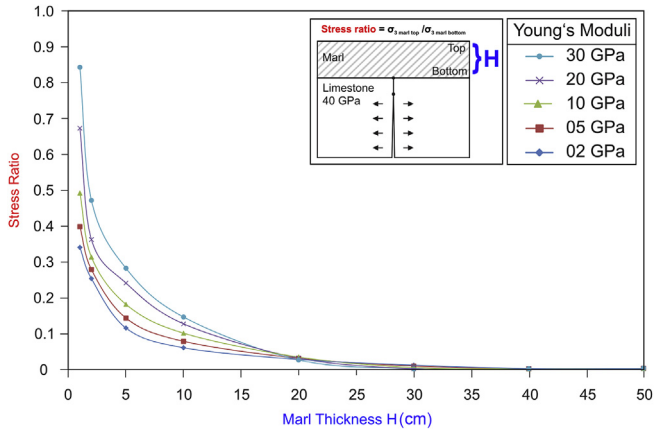

Figure 10. Maximum tensile stress ratio (marl top/marl bottom) versus marl thicknesses (cm). The maximum tensile stress was taken along the contact of the marl top and bottom. The sketch on the right corner shows the undeformed initial stage of the model. Data were separated into five different marl stiffnesses marked by different symbols and colours (see legend).

Fig. 11 shows the impact of different marl stiffnesses in 2 and 5 cm thick marl layers on the stress distribution within the marl. The distribution of the stress field around the fracture tip and the magnitude of tensile stress that reaches the top of the marl layer show remarkable differences between models with 2 cm thick marls (Fig. 11a,c,e) and models with 5 cm thick marls (Fig. 11b,d,f). The distribution of maximum tensile stress along the marl top change from one discrete peak for 2 cm to a wider area along the surface for 5 cm thick marls (see line plot in Fig. 11).

5. Discussion

5.1. Case study of vertical fracture extension

In the field, we observed plumose structures at some fracture planes which is an indication of mode 1 fractures. The term 'joint' is used in field studies for fractures with only slight fracture-normal

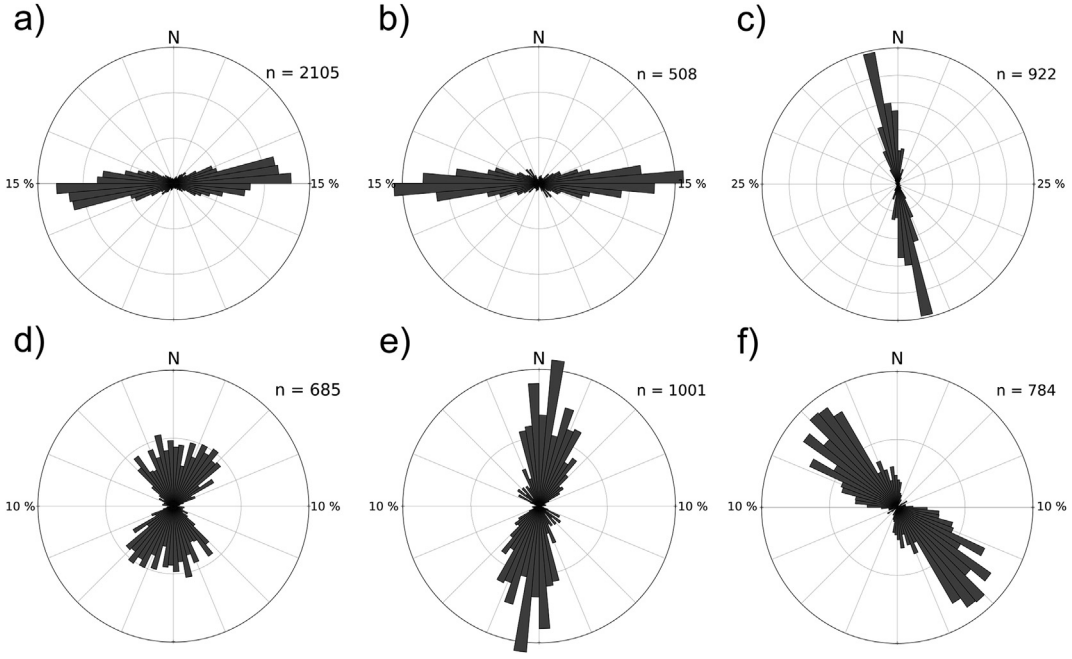

Figure 9. Rose diagrams of all fractures showing in both cases (Wales and Somerset); (a) NP1 (W–E), (b) NP2 (W–E), (c) NP3 (NNW–SSE), (d) KI1 (NNW–SSE, N–S, NNE–SSW), (e) LIL2 (NNE–SSW), (f) KN3 (NW–SE).

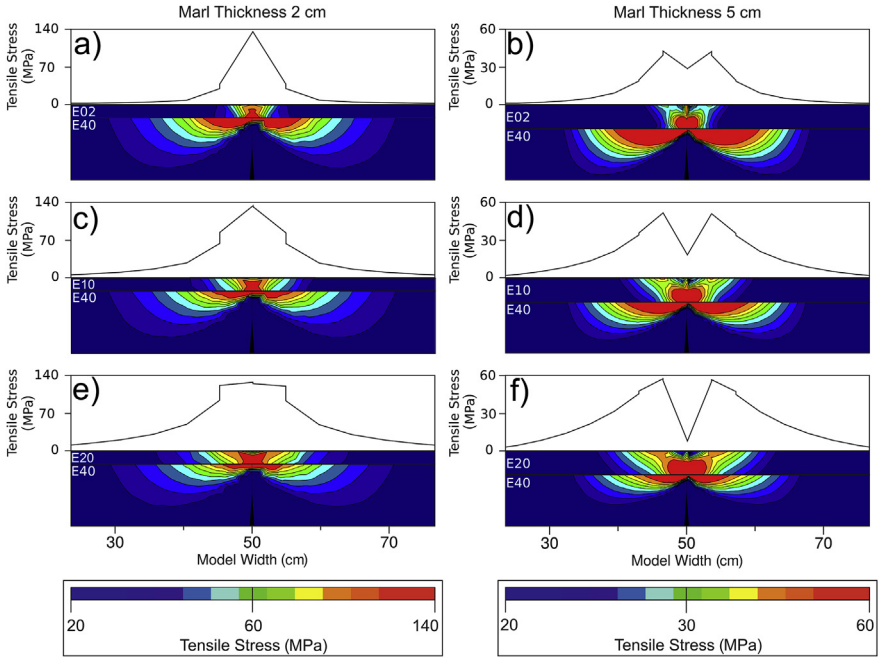

Figure 11. Distribution of the maximum tensile principal stress σ_3 within the layers (contour lines) and along the marl top (line plot) for two different marl thicknesses 2 cm (a,c,e) and 5 cm (b,d,f) as well as different Young's moduli of the marls 2 GPa (a,b), 10 GPa (c,d) and 20 GPa (e,f): (a) H02E02, (b) H05E02, (c) H02E10, (d) H05E10, (e) H02E20, (f) H05E20 (see Table 2 Model setup for details). In this figure only the upper 10 cm of the limestone is illustrated.

displacement and without visible shear displacement (Gudmundsson, 2011).

The measured fracture sets in Wales belong to an orthogonally oriented fracture system, which have been reported in several studies (e.g., Rawnsley et al., 1992, 1998; Caputo, 1995; Pascal et al., 1997). We record the major joint set with systematic fractures (defined based on long and straight trace lengths) in NP3 with a ~170° trend (Fig. 9c), the less planar fractures in NP1 and NP2 strike in ~075° direction (Fig. 9a and b). Latter is abutted against the systematic fractures and have a large step-over along the systematic fractures. The first joint set (~170°) formed during the late Oligocene to Miocene NW–SE compression (Engelder and Peacock, 2001). According to Caputo (1995) both fracture sets (~170° and ~075°) were generated under the same stress field. When the tensile strength is exceeded, fractures occur at right angles to the least principal stress (σ_3) within a biaxial tensile stress field. Caputo (1995) proposes a stress drop in this direction due to stress release, because of this the stress field is locally distorted by a swap between σ_3 and σ_1; when failure conditions in the next cycle are reached, fractures perpendicular oriented to the previous ones were formed. These repeated cycles of failure-events of stress drops and stress swaps can generate these orthogonal fracture sets (Caputo, 1995). The stress swap mechanism takes place locally and is uncoupled by the remote stress field (Caputo, 1995). The rocks in Wales are mainly affected by a series of thrusts and related strike-slip faults. Pascal et al. (1997) describe the regional palaeostress field in Wales with σ_2 sub-vertical, σ_1 and σ_3 sub-horizontal oriented and based on this the authors conclude that the fractures may have been formed during a strike-slip event.

In section KI1 fractures strike within a large scatter from NNW–SSE to NNE–SSW, exhibiting three main fracture sets with NNW–SSE, N–S, and NNE–SSW-strike (Fig. 9d). The fracture sets NNW–SSE and NNE–SSW exhibit the same orientations as a conjugated strike-slip faults documented by Bowyer and Kelly (1995). The sinistral fault has a mean strike of 38° and the dextral fault a mean strike of 315°–05° (Peacock and Sanderson, 1992; Bowyer and Kelly, 1995). The measured fractures in LIL2 strike roughly from 355° to 010° (Fig. 9e). The fractures in KN3 strike ~135°, subparallel to the Quantocks Fault (see Fig. 1a) and represent a systematic fracture set. The rocks in Somerset underwent a more tectonically complicated history (Fig. 1b). For example, reverse faulting was more prevalent in Somerset (Nemčok et al., 1995). This area is separated into distinct fault blocks characterized by differences in both fault strike and fracture patterns (Bowyer and Kelly, 1995). Peacock (2001) pointed out that some joints at East Quantoxhead are interpreted to post-date the normal and strike-slip fault. Discussing how the fractures are linked to these faults in detail goes beyond the scope of this study.

The relation of fracture terminations at limestone-marl contacts with changing marl thicknesses is shown in Fig. 6a. Generally, fracture terminations at limestone-marl contacts show wide spread and do not seem correlated to the thicknesses of marls (Fig. 6a). It seems the nature of contact is more important. Numbers of fracture terminations and crossings along lithological contacts show that most fractures terminate at lithological contacts (Fig. 7a). In many layered rocks, predominantly in sedimentary rocks at shallow depths, the nature of contacts between different lithologies can act as stress barriers (Philipp et al., 2013). The nature of lithological contacts can be mechanically distinguished in (1) welded and (2) weak contacts (Price, 1966; Hobbs, 1967). (1) Welded contacts are strongly cohesive and fractures tend to propagate collinearly through the contacts ('welded-layered model'; Hobbs, 1967). (2) In contrast, at weak contacts, interfacial shear stress directly at the contact occurs and fractures become either arrested or offset and continue side-stepping upwards at the contacts ('slip model'; Price, 1966). Weak contacts might occur when the contrast between Young's modulus of the layer above and below the contact is high. Based on our experience in the field, it is not possible to distinguish welded and weak contacts directly in the field. Not only the difference between welded and weak contact but also the irregularity of the contact is important. Sections with more well-bedded limestones (e.g. in section NP1 marked in blue, Fig. 12a) reveal

higher percentages of fracture terminations at lithological contacts. In contrast, when the lithological contacts tend to be more irregular, which is the case with semi-nodular limestones, fewer fractures terminate at lithological contacts (e.g. in section NP2 marked in red, Fig. 12b; Afşar et al., 2014). In this case, the slip of such weakness planes (i.e. wavy lithological contact) might be disabled and stresses can be better transmitted across these interfaces (Afşar et al., 2014). Fewer fractures propagate over the contact and through the marl layer, as shown in Fig. 7a. However, there is still a substantial number of fractures ($N_{frac\ total} = 2030$) propagate through the contact, which shows a good correlation ($R^2 = 0.76$) between the percentages of fracture extensions (%) and marl thicknesses (m) (Fig. 8a).

5.2. Insights from numerical experiments

The model results show that with increasing marl thickness the stress ratio between the top and bottom of the marl gradually decreases (Fig. 10). Most fractures would propagate through <20 cm marls, however, in >40 cm thick marls no tensile stress reaches the top of the marl and consequently no fracture would propagate. Model experiments also show that the higher the contrast in stiffness between limestone and marl layers, the lower the stress that is transmitted into the marl layer, independent of its thickness (see in Figs. 10 and 11a,b). Therefore, in the case of a high stiffness contrast between limestone and marl, the contact acts as a stress barrier. A more detailed view of the tensile stress distribution for all model experiments show, that a single location of greatest tension occurs along the top surface of the marl directly in front of the fracture, but only in 1 cm thick marls (blue line in Fig. 13a–d). The same stress distribution is observable in 2 cm thick marls, however, only for softer marls (E <−20 GPa; Fig. 11, the red line in Fig. 13a and b). Two locations of greatest principal tension along the surface top of the marl, one each side of the fracture tip are most pronounced in 5 cm thick marls with different Young's moduli (yellow line in Fig. 13). In a similar study, the effect of different strength bonded contacts was investigated, while they changed the distance from the fracture tip to the interface and the nature of the interface (Cooke and Underwood, 2001). The results show two pronounced peaks at maximum tensile stress in cases of weak contacts. Strongly bonded contacts, however, show only one pronounced peak directly in front of the fracture tip. In our study, the condition of the interface is the same only the marl thickness and stiffness is changing.

5.3. Comparison of field data and models

The field data show the state of the fractured rock, whereas the numerical experiments were used to examine the potential of fracture extension. Although field observations give good insights on stress barriers in layered rocks, sedimentary layers are internally extremely heterogeneous (e.g. bioturbation, lamination). In contrast, numerical experiments with homogeneous layers give noise-free results and a better understanding of potential stress barriers. Our field data demonstrate a clear correlation between the percentage of non-stratabound fractures and marl thicknesses (Fig. 8). The relative proportion of non-stratabound fractures strongly decreases at bed thicknesses exceeding 15 cm (Fig. 8a). This trend might be slightly imbalanced as most beds have thicknesses of <20 cm (Fig. 14, light grey). However, it is corroborated by our numerical model results, which show that in marls thicker than 20 cm considerably less tensile stress reaches the top of these marl than for marls thinner than 20 cm (see stress ratio of top to bottom in Fig. 10). Considering both results from field and model data we consider therefore a critical marl thickness of ca. 15–20 cm as plausible. Models in a chalk-shale system show a critical shale thickness of 20 cm for an underlying 1 m thick chalk layer (Rijken and Cooke, 2001). The model results show also that the higher the contrast between limestone and marl stiffness (e.g. dark blue and red line) the lower the stress that is transmitted through the marl layer (see stress ratio), independent of its thickness (see marl thickness from 1 cm to 10 cm in Fig. 10). The maximum tensile stress distribution of the models shows different distributions from one pronounced peak occurring in model series with a soft and thin marl layer (Fig. 13). The one peak stress concentration can be interpreted as a straight propagated fracture. In contrast, very soft marls with a thickness of 5 cm show two stress peaks shifted from the original fracture tip (Fig. 13). In this case, stresses are transmitted across the interface to either side of the fracture and may produce a step-over fracture. In this field study, step-over fractures were considered as two different fractures, that might be the reason why most of the fractures terminate at contacts and why the termination at the contact are not directly linked to the marl thickness. The field data might be overestimated in regards of fracture termination.

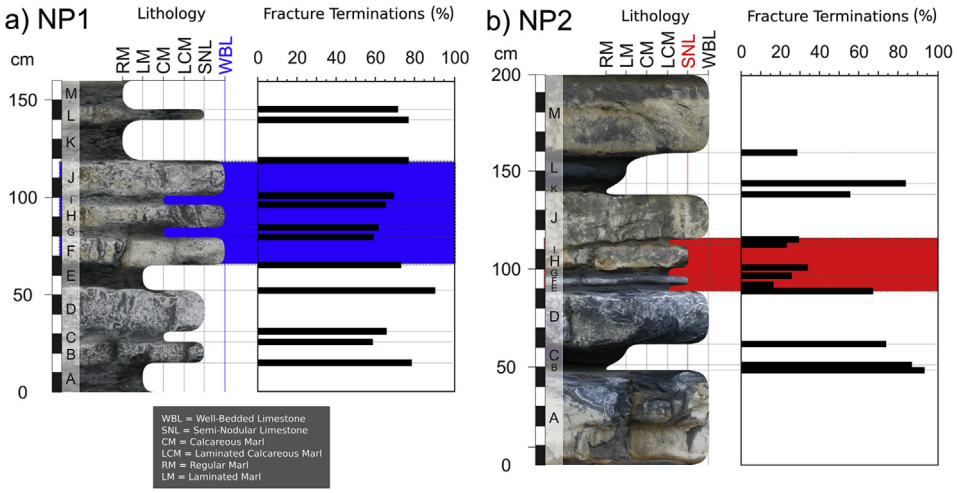

Figure 12. Sedimentological logs (break-off illustrates differences in lithology see the legend), percentages of fracture terminations at contacts; (a) section NP1, (b) NP2 (see Table 1 for lithology details). Please note that both sections represent different stratigraphic intervals within the Blue Lias Formation.

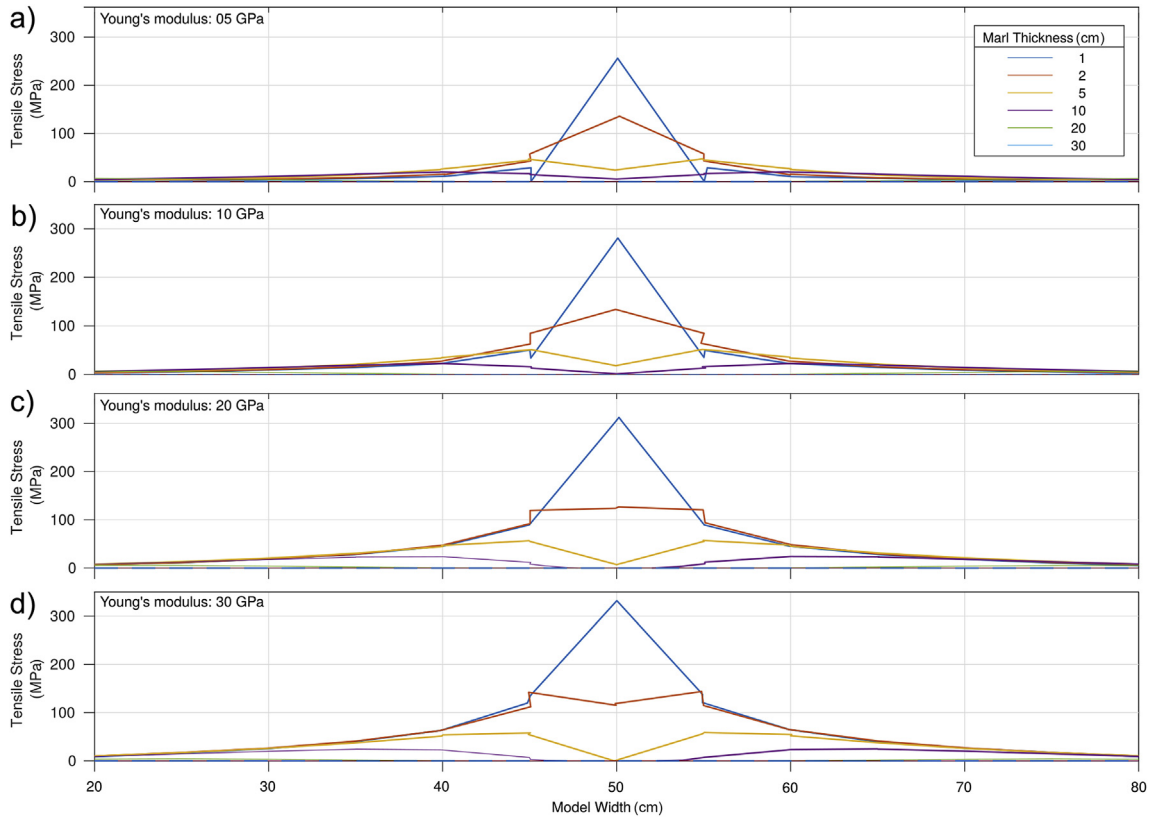

Figure 13. Distribution of maximum tensile stress along the marl top with changing marl thicknesses and changing Young's moduli; (a) 05, (b) 10, (c) 20, (d) 30 GPa.

6. Conclusions

Vertical fracture extension in layered reservoirs tend to be restricted to impermeable layers like marls. The quantification of critical marl thicknesses improve the construction of more complete models of these reservoirs. This study focused on a systematic investigation of the link between fracture extension and impermeable layers. Most of the fractures mapped in the field terminate at limestone-marl contacts, however, the terminations at the contact are not directly linked to the marl thickness. It seems the nature of the contact (welded vs. weak contact, planar vs. wavy contact) is more important. The extension of fractures through the marl layer is, however, strongly correlated with marl thickness. Field data shows a good correlation ($R^2 = 0.76$) between fracture extension and marl thickness, the thicker the marl layer the lower the number of fractures that propagate through. This agrees well with the model results, in both model experiments and field data the critical marl thickness for fracture extension is ca. 15–20 cm. For marls in the models that are less than 20 cm, more tensile stress reaches the marl top. However, for marls with the same thickness but less than 20 cm, the contrast between limestone and marl stiffness has a stronger impact. That means the higher the contrast between limestone and marl stiffness the lower the stress that is transmitted into the marl layer with the same thickness. This is because, in very soft marls for example (Young's modulus of 2 GPa) with a thickness of 5 cm, stresses are transmitted across the interface to either side of the fracture tip, which can be interpreted as step-over fractures along contacts. In concert, our findings demonstrate that vertical fracture extension in limestone-marl alternation is controlled by less than 20 cm thick marl layers. This must be considered for different permeability upscaling techniques to improve not only well performance but also to construct more complete reservoirs models.

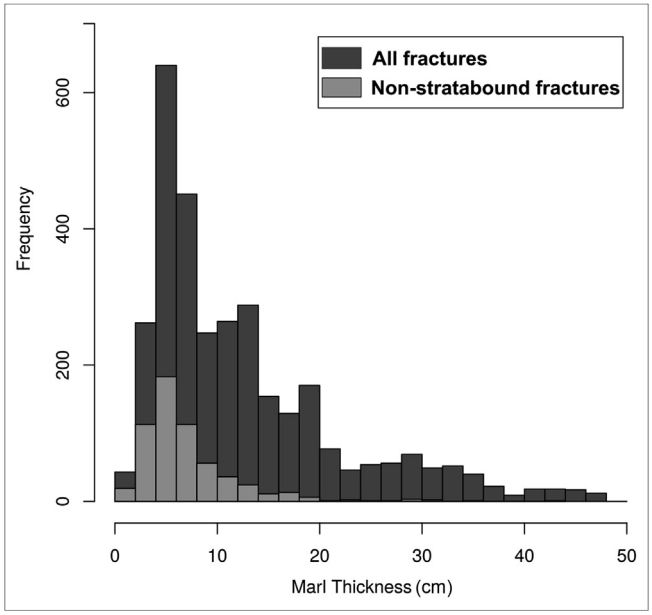

Figure 14. The histogram shows the frequency of marl thicknesses measured along with all fractures in dark grey and for only non-stratabound fractures in light grey.

Acknowledgments

This study was supported by the Deutsche Forschungsgemeinschaft (DFG, grant PH 189/2-1). We thank Sonja

Philipp and Hildegard Westphal for constructive discussions and providing laboratory instruments. Jan-Peter Duda is acknowledged for assistance in the field. We thank also the reviewers John Cosgrove and one anonymous reviewer as well as the Guest Editors Vinod Samuel, Silvia Japas and Sebastián Oriolo for critical comments.

References

Afşar, F., Westphal, H., Philipp, S.L., 2014. How facies and diagenesis affect fracturing of limestone beds and reservoir permeability in limestone-marl alternations. Marine and Petroleum Geology 57, 418–432.

Aguilera, R., 2000. Well test analysis of multi-layered naturally fractured reservoirs. Journal of Canadian Petroleum Technology 39 (07).

Beasy, 1991. The Boundary Element Analysis System User Guide. Computational Mechanics. BEASY Manual Boston. http://www.beasy.com.

Belayneh, M., Cosgrove, J.W., 2010. Hybrid veins from the southern margin of the Bristol Channel basin, UK. Journal of Structural Geology 32, 192–201.

Bowyer, M., Kelly, P., 1995. Strain and scaling relationships of faults and veins at Kilve, Somerset. Proceedings of the Ussher Society 8, 411-411.

Brebbia, C.A., Dominguez, J., 1994. Boundary Elements: an Introductory Course. WIT press.

Brenner, S.L., Gudmundsson, A., 2004. Permeability in layered reservoirs: field examples and models on the effects of hydrofracture propagation. In: Stephansson, O., Hudson, J.A., Jing, L. (Eds.), Coupled Thermo-Hydro-Mechanical-Chemical Processes in Geo-Systems. Geo-EngineeringBook Series, vol. 2. Elsevier, pp. 643–648.

Brooks, M., Trayner, P.M., Trimble, T.J., 1988. Mesozoic reactivation of variscan thrusting in the Bristol Channel area, UK. Journal of the Geological Society 145 (3), 439–444.

Caputo, R., 1995. Evolution of orthogonal sets of coeval extension joints. Terra Nova 7, 479–490.

Cooke, M.L., Underwood, C.A., 2001. Fracture termination and step-over at bedding interfaces due to frictional slip and interface opening. Journal of Structural Geology 23 (2), 223–238.

Cornford, C., 1986. The Bristol Channel Graben: organic geochemical limits on subsidence and speculation on the origin of inversion. Proceedings of the Ussher Society 6 (3), 360–367.

Cox, B.M., Sumbler, M.G., Ivimey-Cook, H.C., 1999. A formational framework for the lower Jurassic of England and Wales (onshore area). Tech. rep. Research report, Number RR/99/01, Keyworth, Nottingham, 1–30.

Dart, C.J., McClay, K., Hollings, P.N., 1995. 3D analysis of inverted extensional fault systems, southern Bristol Channel basin, UK. Geological Society, London, Special Publications 88 (1), 393–413.

Donovan, D.T., Horton, A., Ivimey-Cook, H.C., 1979. The transgression of the lower Lias over the northern flank of the London platform. Journal of the Geological Society 136, 165–173.

Dunham, R.J., 1962. Classification of carbonate rocks according to depositional textures. In: Hamm, W.E. (Ed.), Classification of Carbonate Rocks-A Symposium. American Association of Petroleum Geologists, Tulsa, Oklahoma, pp. 108–121.

Dvorkin, J., Walls, J.D., Mavko, G., 2005. Rock physics of marls. In: SEG Technical Program Expanded Abstracts 2001. Society of Exploration Geophysicists, pp. 1784–1787.

Economides, M.J., Nolte, K.G., 2000. Reservoir Stimulation, third ed. Wiley, New York. 808 pp.

Engelder, T., Peacock, D.C.P., 2001. Joint development normal to regional compression during flexural-flow folding: the Lilstock buttress anticline, Somerset, England. Journal of Structural Geology 23 (2), 259–277.

Gale, J.F., Laubach, S.E., Olson, J.E., Eichhubl, P., Fall, A., 2014. Natural fractures in shale: a review and new observations natural fractures in shale: a review and new observations. AAPG Bulletin 98 (11), 2165–2216.

Gudmundsson, A., 2011. Rock Fractures in Geological Processes. Cambridge University Press.

Harvey, T., Gray, J., 2013. The unconventional hydrocarbon resources of Britains onshore basin shale gas. Rep. Dept. Energy and Climate Change. UK, 1–40.

Hobbs, D.W., 1967. The formation of tension joints in sedimentary rocks: an explanation. Geological Magazine 104, 550–556.

Hobbs, P., Entwisle, D., Northmore, K., Sumbler, M., Jones, L., Kemp, S., Self, S., Barron, M., Meakin, J., 2012. Engineering geology of British rocks and soils: Lias Group. Tech. rep. British Geological Survey, 1–323.

Hoorn, B.V., 1987. The south Celtic Sea/Bristol Channel Basin: origin, deformation and inversion history. Tectonophysics 137 (1), 309–334.

Hudson, J.A., Harrison, J.P., 2000. In situ stress. In: Hudson, J.A., Harrison, J.P. (Eds.), Engineering Rock Mechanics: An Introduction to the Principles. Pergamon, Oxford, pp. 41–69.

Hudson, J.A., Cornet, F.H., Christianson, R., 2003. ISRM suggested methods for rock stress estimation Part 1: strategy for rock stress estimation. International Journal of Rock Mechanics and Mining Sciences 40 (7), 991–998.

Jaeger, J.C., Cook, N.G.W., Zimmermann, R.W., 2007. Fundamentals of Rock Mechanics, fourth ed. Blackwell, Oxford. 488 pp.

Kamerling, P., 1979. The geology and hydrocarbon habitat of the Bristol Channel Basin. Journal of Petroleum Geology 2 (1), 75–93.

Larsen, B., Gudmundsson, A., 2010. Linking of fractures in layered rocks: implications for permeability. Tectonophysics 492, 108–120.

Mitchell, R., 2006. Petroleum engineering handbook, volume II: drilling engineering. Society of Petroleum Engineers, 1–763.

National Research Council, N.R., 1996. Rock Fractures and Fluid Flow: Contemporary Understanding and Applications. The National Academies Press, Washington, DC, 568 pp.

Nemčok, M., Gayer, R., Miliorizos, M., 1995. Structural analysis of the inverted Bristol Channel Basin: implications for the geometry and timing of fracture porosity. In: Buchanan, J.G., Buchanan, P.G. (Eds.), Basin Inversion. Geological Society, London, Special Publications 88 (1), pp. 355-392.

Pascal, C., Angelier, J., Cacas, M.-C., Hancock, P.L., 1997. Distribution of joints: probabilistic modeling and case study near Cardiff (Wales, U.K.). Journal of Structural Geology 19 (10), 1273–1284.

Peacock, D.C.P., Sanderson, D.J., 1992. Effects of layering and anisotropy on fault geometry. Journal of the Geological Society 149 (5), 793–802.

Peacock, D., 2001. The temporal relationship between joints and faults. Journal of Structural Geology 23, 329–341.

Philipp, S.L., Afşar, F., Gudmundsson, A., 2013. Effects of mechanical layering on hydrofracture emplacement and fluid transport in reservoirs. Frontiers of Earth Science 1, 4.

Portela, A., Aliabadi, M.H., Rooke, D.P., 1993. Dual boundary element incremental analysis of crack propagation. Computers & Structures 46 (2), 237–247.

Price, N.J., 1966. Brittle fracture. In: Price, N.J. (Ed.), Fault and Joint Development in Brittle and Semi-brittle Rock. The Commonwealth and International Library: Geology Division. Pergamon, pp. 1–56.

Qi, D., Hesketh, T., 2005. An analysis of upscaling techniques for reservoir simulation. Petroleum Science and Technology 23 (7–8), 827–842.

Rawnsley, K.D., Rives, T., Petti, J.-P., Hencher, S.R., Lumsden, A.C., 1992. Joint development in perturbed stress fields near faults. Journal of Structural Geology 14 (8), 939–951.

Rawnsley, K.D., Peacock, D.C.P., Rives, T., Petit, J.-P., 1998. Joints in the Mesozoic sediments around the Bristol Channel basin. Journal of Structural Geology 20 (12), 1641–1661.

Reeves, G.M., Sims, I., Cripps, J., 2006. Clay materials used in construction. Geological Society of London, 1–473.

Rijken, P., Cooke, M.L., 2001. Role of shale thickness on vertical connectivity of fractures: application of crack-bridging theory to the Austin Chalk, Texas. Tectonophysics 337 (1), 117–133.

Roche, V., Baan, M.V.D., 2013. Numerical modeling of the role of lithological layering on spatial variation of natural and induced fractures and their nucleation. In: SEG Technical Program Expanded Abstracts 2013, pp. 2188–2192.

Rozell, D.J., Reaven, S.J., 2012. Water pollution risk associated with natural gas extraction from the Marcellus Shale. Risk Analysis: International Journal 32 (8), 1382–1393.

Somerset County Council, 2017. Oil and Gas Development. Last update 7 June 2017. http://www.somerset.gov.uk/policies-and-plans/policies/oil-and-gas/.

Stewart, S.A., Ruffell, A.H., Harvey, M.J., 1997. Relationship between basement-linked and gravity-driven fault systems in the UKCS salt basins. Marine and Petroleum Geology 14 (5), 581–604.

Tappin, D.R., Chadwick, R.A., Jackson, A.A., Wingfield, R.T.R., Smith, N.J.P., 1994. The geology of cardigan bay and the Bristol Channel. British Geological Survey, 1–104.

Whittaker, A., Green, G.W., 1983. Geology of the country around Westonsuper-Mare. Geological Survey of Great Britain, Institute of Geological Sciences, Her Majesty's Stationary Office, London, 1–147.

Wilson, D., 1990. Geology of the South Wales Coalfield, Part VI, the Country Around Bridgend. No. 261 in 262. Bernan Press (PA), 53 pp.

Yilmaz, Ö., 2001. Seismic Data Analysis. Society of Exploration Geophysicists, 454 pp.

Zeeb, C., Gomez-Rivas, E., Bons, P.D., Blum, P., 2013. Evaluation of sampling methods for fracture network characterization using outcrops. AAPG Bulletin 97 (9), 1545–1566.

Zoback, M.D., 2007. Reservoir Geomechanics. Cambridge University Press, 505 pp.

Zoback, M., Kitasei, S., Copithorne, B., 2010. Addressing the Environmental Risks from Shale Gas Development, vol. 21. Worldwatch Institute, Washington, DC.